



**HAL**  
open science

## **JWST Imaging of Edge-on Protoplanetary Disks. III. Drastic Morphological Transformation Across the Mid-infrared in Oph163131**

Marion Villenave, Karl R. Stapelfeldt, Gaspard Duchêne, François Ménard,  
Marshall D. Perrin, Christophe Pinte, Schuyler G. Wolff, Ryo Tazaki,  
Deborah L. Padgett

► **To cite this version:**

Marion Villenave, Karl R. Stapelfeldt, Gaspard Duchêne, François Ménard, Marshall D. Perrin, et al.. JWST Imaging of Edge-on Protoplanetary Disks. III. Drastic Morphological Transformation Across the Mid-infrared in Oph163131. *The Astrophysical Journal*, 2024, 975, 10.3847/1538-4357/ad7de0 . insu-04836783

**HAL Id: insu-04836783**

**<https://insu.hal.science/insu-04836783v1>**

Submitted on 13 Dec 2024

**HAL** is a multi-disciplinary open access archive for the deposit and dissemination of scientific research documents, whether they are published or not. The documents may come from teaching and research institutions in France or abroad, or from public or private research centers.





L'archive ouverte pluridisciplinaire **HAL**, est destinée au dépôt et à la diffusion de documents scientifiques de niveau recherche, publiés ou non, émanant des établissements d'enseignement et de recherche français ou étrangers, des laboratoires publics ou privés.



Distributed under a Creative Commons Attribution 4.0 International License



# JWST Imaging of Edge-on Protoplanetary Disks. III. Drastic Morphological Transformation Across the Mid-infrared in Oph163131

Marion Villenave<sup>1,2</sup> , Karl R. Stapelfeldt<sup>2</sup> , Gaspard Duchêne<sup>3,4</sup> , François Ménard<sup>4</sup> , Marshall D. Perrin<sup>5</sup> ,  
Christophe Pinte<sup>4,6</sup> , Schuyler G. Wolff<sup>7</sup> , Ryo Tazaki<sup>4</sup> , and Deborah L. Padgett<sup>2</sup> 

<sup>1</sup> Università degli Studi di Milano, Dipartimento di Fisica, via Celoria 16, 20133 Milano, Italy; [marion.villenave@unimi.it](mailto:marion.villenave@unimi.it)

<sup>2</sup> Jet Propulsion Laboratory, California Institute of Technology, 4800 Oak Grove Drive, Pasadena, CA 91109, USA

<sup>3</sup> Astronomy Department, University of California, Berkeley, CA 94720, USA

<sup>4</sup> Université Grenoble Alpes, CNRS, IPAG, F-38000 Grenoble, France

<sup>5</sup> Space Telescope Science Institute, Baltimore, MD 21218, USA

<sup>6</sup> School of Physics and Astronomy, Monash University, Clayton Vic 3800, Australia

<sup>7</sup> Department of Astronomy and Steward Observatory, University of Arizona, Tucson, AZ 85721, USA

Received 2024 July 11; revised 2024 September 12; accepted 2024 September 19; published 2024 November 6

## Abstract

We present JWST broadband images of the highly inclined protoplanetary disk SSTc2d J163131.2-242627 (Oph163131) from 2.0 to 21  $\mu\text{m}$ . The images show a remarkable evolution in disk structure with wavelength, quite different from previous JWST observations of other edge-on disks. At 2.0 and 4.4  $\mu\text{m}$ , Oph163131 shows two scattering surfaces separated by a dark lane, typical of highly inclined disks. Starting at 7.7  $\mu\text{m}$ , however, (1) the two linear nebulosities flanking the dark lane disappear; (2) the brighter nebula tracing the disk upper surface transitions into a compact central source distinctly larger than the JWST point-spread function and whose intrinsic size increases with wavelength; and (3) patches of extended emission appear at low latitudes, and at surprisingly large radii nearly twice that of the scattered light seen with Hubble Space Telescope and NIRCam, and of the gas. We interpret the compact central source as thermal emission from the star and the inner disk that is not seen directly, but which instead is able to progressively propagate to greater distances at longer wavelengths. The lack of sharp-edged structures in the extended patchy emission argues against the presence of shocks and suggests photoexcitation or stochastic heating of material smoothly flowing away from the star along the disk surface. Finally, the dark lane thickness decreases significantly between 0.6 and 4.4  $\mu\text{m}$ , which indicates that the surface layers of Oph163131 lack grains larger than 1  $\mu\text{m}$ .

*Unified Astronomy Thesaurus concepts:* [Protoplanetary disks \(1300\)](#); [Planet formation \(1241\)](#); [Radiative transfer \(1335\)](#); [Dust continuum emission \(412\)](#)

## 1. Introduction

Planets are built from the growth of submicron-sized particles that evolve into larger bodies within protoplanetary disks. A full understanding of this process requires a detailed characterization of the radial and vertical structure of disks. Indeed, the level of dust concentration within a disk plays an important role in the local grain growth (e.g., T. Birnstiel et al. 2012) and planetesimal formation efficiency (e.g., A. N. Youdin & Y. Lithwick 2007; M. Lambrechts & A. Johansen 2012). Pressure maxima can trap and concentrate dust radially, while size-dependent vertical settling concentrates dust vertically. These mechanisms can provide favorable conditions for rapid grain growth but remain to be fully characterized.

Protoplanetary disks viewed edge-on provide a unique opportunity to study their vertical structure since it is directly visible. Previous observations with the Hubble Space Telescope (HST) revealed that, in the optical and near-infrared, edge-on protoplanetary disks appear as two reflection nebulae separated by a dark lane (e.g., C. J. Burrows et al. 1996; A. M. Watson et al. 2007). When observed at multiple scattered light wavelengths, the thickness of the dark lane can provide insight into the dust properties and disk vertical structure.

Pioneering studies in three edge-on disks observed between 0.6 and 5  $\mu\text{m}$  (HH 30, HV Tau C, HK Tau B; A. S. Coiera et al. 2001; A. M. Watson & K. R. Stapelfeldt 2004; G. Duchêne et al. 2010; C. McCabe et al. 2011) have shown that the dark lane thickness tends to decrease with wavelength. This indicates either a vertically uniform distribution of grain sizes whose dust opacity strongly decreases with wavelength, or a vertically stratified dust distribution with the larger grains settled nearer to the midplane.

The James Webb Space Telescope (JWST), with its much higher sensitivity in the mid-infrared, allows such studies to be extended to more systems. JWST also brings a larger range of wavelengths within reach by allowing the detection of scattered light out to  $\sim 20 \mu\text{m}$ , which is extremely difficult from the ground. This is the third paper based on an ongoing JWST near- to mid-infrared imaging campaign targeting some of the largest edge-on disks in nearby star-forming regions (GO programs 2562 and 4290 in Cycles 1 and 2, co-PIs: F. Ménard and K. R. Stapelfeldt). The goal of this program is to investigate dust evolution mechanisms such as dust vertical settling and grain growth, in particular through the wavelength evolution of their dark lane thickness. The first two papers of this series focused on the Class II disk Tau042021 (G. Duchêne et al. 2024) and the Class I disk IRAS 04302 (M. Villenave et al. 2024). In both systems, the dark lane thickness does not vary significantly with wavelength across the mid-infrared, which indicates that vertical settling is not taking place for



Original content from this work may be used under the terms of the [Creative Commons Attribution 4.0 licence](#). Any further distribution of this work must maintain attribution to the author(s) and the title of the work, journal citation and DOI.

grains  $\lesssim 10 \mu\text{m}$  in size. The last target of the JWST cycle 1 program, the Class II HH 30, will be analyzed in Tazaki et al. (2024, Submitted).

In addition to allowing the study of dust vertical settling, the new JWST observations also revealed other unexpected and remarkable disk features. For example, a surprising switch in the brightest nebulae with wavelength in IRAS 04302 suggested that this disk could possess a tilted inner region. Their models including a tilted inner region also predict lateral asymmetries in the scattering nebulae when observed with the right orientation. Because lateral asymmetries are seen in a large number of edge-on disks, M. Villenave et al. (2024) suggested that tilted inner disks might be common in protoplanetary disks. This is consistent with shadows identified in scattered light observations of lower inclination systems (e.g., M. Benisty et al. 2023, for a review), and could be caused by misaligned companion (e.g., S. Facchini et al. 2013) or late infall (e.g., M. Kuffmeier et al. 2021). Finally, in the case of Tau042021, outflow structures well away from the disk plane were seen. The clear X-shape feature detected in the broadband observations (G. Duchêne et al. 2024) was also identified in H<sub>2</sub> and PAH lines (N. Arulanantham et al. 2024) and has been interpreted as part of a disk wind.

The focus of this work is the Class II edge-on protoplanetary disk SSTc2dJ163131.2-242627 (hereafter Oph163131). The system was identified on the basis of its double-peaked spectral energy distribution in the Spitzer c2d survey (N. J. Evans et al. 2009), and confirmed as an edge-on disk with HST imaging by K. R. Stapelfeldt et al. (2014). It has been the target of detailed studies at several wavelengths, going from the optical, near-infrared to the millimeter, both in dust and gas. The millimeter dust of this disk is found to be significantly affected by vertical settling, indicating particularly weak turbulence (S. G. Wolff et al. 2021; M. Villenave et al. 2022). The 2D temperature structure of the disk revealed that the cold disk midplane is flanked by warmer CO gas at the disk’s upper and lower surfaces. At large radii, however, the CO is found to be vertically isothermal, which might be related to external UV irradiation of the disk (C. Flores et al. 2021). Finally, contrary to IRAS 04302, which has an envelope (S. Wolf et al. 2003; M. Villenave et al. 2024), or Tau042021, which has a clear jet and winds (N. Arulanantham et al. 2024; G. Duchêne et al. 2024), no spectroscopic signatures of accretion or outflow were identified in Oph163131 (C. Flores et al. 2021), making this source akin to weak-line T Tauri stars and thus possibly the most evolved disk target in our JWST cycle 1 program.

Here, we extend the study of this system to the mid-infrared, aiming to understand the spatial distribution of intermediate-sized particles. We present the observations in Section 2. Descriptions of the images are shown in Section 3 and discussed along with illustrative models in Section 4. Finally, we summarize our findings in Section 5.

## 2. Observations and Data Reduction

We observed Oph163131 with JWST (GO program 2562, PIs F. Ménard & K. Stapelfeldt) using both NIRCcam and MIRI instruments in two consecutive visits starting on 2023 March 7 UT 19:56. The observations used five different filters, F200W (2.0  $\mu\text{m}$ ), F444W (4.44  $\mu\text{m}$ ), F770W (7.7  $\mu\text{m}$ ), F1280W (12.8  $\mu\text{m}$ ), and F2100W (21.0  $\mu\text{m}$ ). The two NIRCcam images were obtained simultaneously with exposures of 773 s. The MIRI observations were taken successively with exposures of

840 s at 7.7  $\mu\text{m}$ , 855 s at 12.8  $\mu\text{m}$ , and 661 s at 21  $\mu\text{m}$ , respectively.

For the F200W, F770W, F1280W, and F2100W observations, we obtained the phase 2 pipeline calibrated data from the MAST archive<sup>8</sup>, and we reran phase 3, using the JWST pipeline version 1.9.5. In the `skymatch` step, we used the default `skymethod` “global+match” but set `subtract=True`. The subtracted background levels were 0.49, 15.76, 48.63, and 271.98 MJy sr<sup>-1</sup> in F200W, F770W, F1280W, and F2100W, respectively. For the MIRI images, we also performed an additional 2D background subtraction step using the `Background2D` function in the `photutils` Python package.

For the F444W observations, we obtained the uncalibrated data from the archive and reran each pipeline step using pipeline version 1.11.1.dev16+gb79a88af. In order to recover saturated pixels, we set `suppress_one_group=False` in the `ramp fit` step of phase 1. This allows us to suppress the ramp fit in the case when only the 0th group is unsaturated. We use the default pipeline values in phases 2 and 3, except for the `skymatch` step, where we subtract the background. The subtracted background level in F444W was 0.65 MJy sr<sup>-1</sup>.

Finally, we resampled and aligned each image to the NIRCcam F200W pixel size and position. We adopt the `reproject` Python package to resample the images, and align them using a background galaxy visible in all fields and previously anchored to its position, as given in the GAIA DR3 catalog (Gaia Collaboration et al. 2021) accessed through the Aladin Sky Atlas (F. Bonnarel et al. 2000; M. Baumann et al. 2022). We visually checked that the alignment does not require a rotation; it only includes a shift in R.A. and decl. The final images are presented in Figures 1 and 2, and a three-color composite image is displayed in Figure 3.

In this work, we also use the Advanced Camera for Surveys (ACS)/Wide Field Channel images from the HST Archive (program 12514, PI: K. Stapelfeldt). The HST observations were obtained using filters F606W and F814W (0.6, 0.8  $\mu\text{m}$ ) and observed on 2012 March 4. They were previously published by S. G. Wolff et al. (2021).

## 3. Results

In Figure 1, we show the NIRCcam and HST observations of Oph163131 (0.6–4.44  $\mu\text{m}$ ). At these wavelengths, the disk shows two scattered light nebulae separated by a dark lane, typical of edge-on protoplanetary disks. We adopt the methodology previously employed by G. Duchêne et al. (2024) and M. Villenave et al. (2024) to fit the two scattering surfaces and quantify disk parameters. In short, this method finds a “spine” for the two disk-scattering surfaces. To do so, it first derives the vertical position of the scattering surfaces as a function of radius (i.e., distance from the symmetry axis) defined as the peaks in cuts along the minor axis direction. Those are then fitted by a polynomial function to define the spines. We refer to these works for the full description of the methodology. We infer the dark lane thickness ( $d_{\text{neb}}$ ), radial full width at half-maximum ( $R_{\text{FWHM}}$ ), and the radial full width at 10% of the peak ( $R_{10\%}$ ) of each spine. In addition, we also estimate the integrated flux ratio between the top and bottom nebulae, using aperture photometry. The results are summarized in Table 1.

<sup>8</sup> doi:10.17909/zrsp-nc48

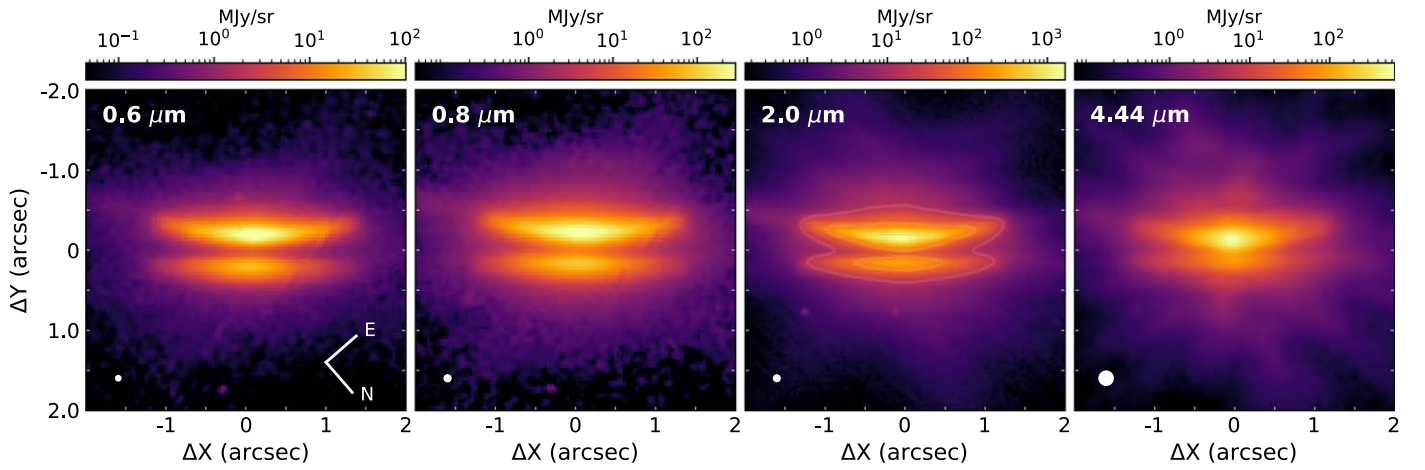


**Figure 1.** HST/ACS (0.6, 0.8  $\mu\text{m}$ ) and JWST/NIRCam (2.0, 4.44  $\mu\text{m}$ ) images of Oph163131, rotated so that the brighter southeast nebula is up. The white ellipse in the bottom left of each panel represents the resolution of the observations. On the third panel, the faint white contours correspond to 15 and 100  $\text{MJy sr}^{-1}$  levels in the 2.0  $\mu\text{m}$  NIRCam image.

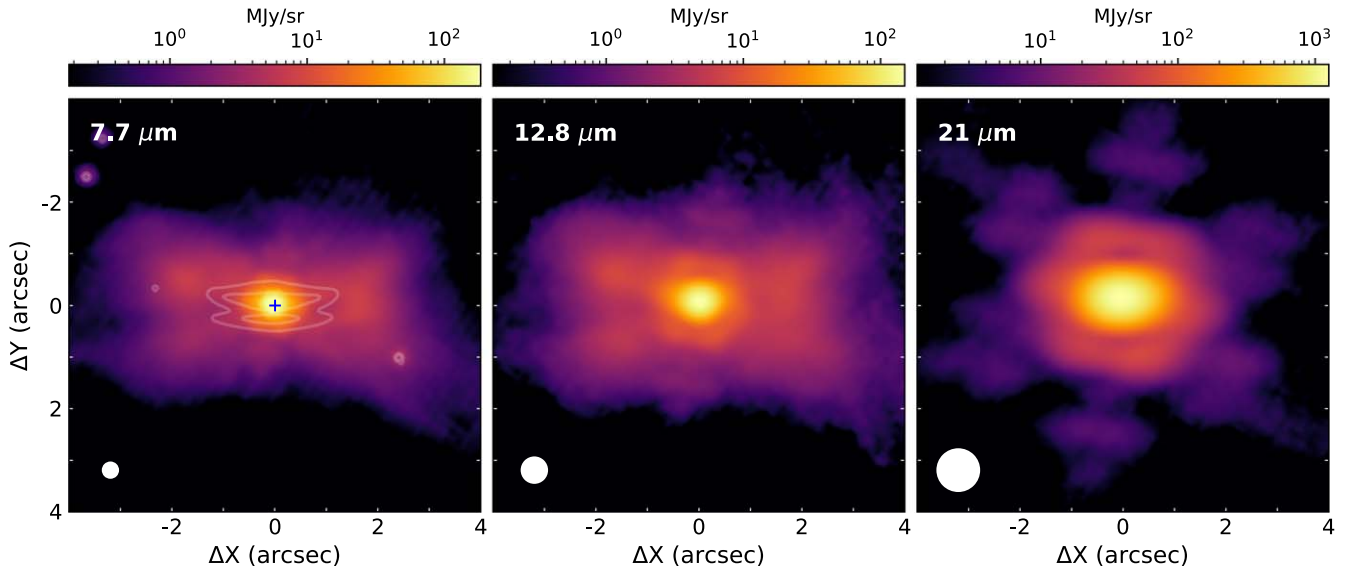


**Figure 2.** JWST/MIRI images of Oph163131. While the orientation is the same as in Figure 1, the field of view is twice as large. On the leftmost panel, the white contours correspond to 15 and 100  $\text{MJy sr}^{-1}$  levels in the 2.0  $\mu\text{m}$  NIRCam image (same as in Figure 1), and the dark cross shows the location of the brightest pixel at 7.7  $\mu\text{m}$ . The resolution of the observations is shown as white ellipses in the bottom left corner.

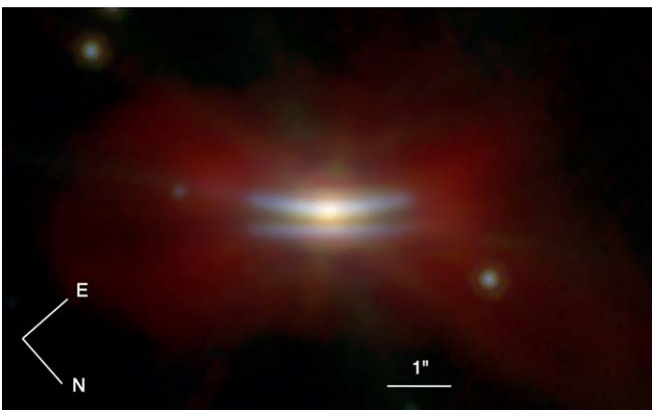


**Figure 3.** JWST three-color composite image of Oph163131; the full field of view spans  $10'' \times 6''$ . The 2.0, 4.44, and 7.7  $\mu\text{m}$  images are rendered (using a logarithmic stretch) in the blue, green, and red channels, respectively.

We find that the dark lane thickness  $d_{\text{neb}}$  of Oph163131 decreases by a factor of 2 between 0.6 and 4.44  $\mu\text{m}$ . While the radial extent of the top and bottom nebula are similar within  $3\sigma$ , both become more centrally peaked at 4.44  $\mu\text{m}$ . The integrated flux ratio between the top and bottom nebulae increases with wavelength.

We show the observations obtained with MIRI, from 7.7 to 21  $\mu\text{m}$ , in Figure 2. The morphology of the source is dramatically different at these wavelengths. Figure 3 shows a three-color composite image highlighting the major changes in the appearance of the source between NIRCam and MIRI wavelengths. At the longer wavelengths, the two disk-scattering surfaces become invisible, and instead, the images display a bright central source resolved along the disk's major axis. We measured the size of this central source by fitting a 2D Gaussian using the IDP3 routines in IDL, comparing the observed source size to *Webb*PSF models (M. D. Perrin et al. 2014) for a point source in each of the three MIRI filters. After



**Table 1**  
Oph163131 Morphological Properties

$\lambda$ ( $\mu\text{m}$ )	$d_{\text{neb}}$ ( $''$ )	$\text{FR}_{\text{integrated}}$ T/B	$R_{\text{FWHM}}$ B ( $''$ )	$R_{\text{FWHM}}$ T ( $''$ )	$R_{\text{FW10\%}}$ B ( $''$ )	$R_{\text{FW10\%}}$ T ( $''$ )
0.6	$0.42 \pm 0.01$	3.0	$0.93 \pm 0.11$	$0.82 \pm 0.11$	$1.88 \pm 0.08$	$1.86 \pm 0.05$
0.8	$0.40 \pm 0.01$	3.3	$0.99 \pm 0.12$	$0.92 \pm 0.12$	$2.00 \pm 0.04$	$1.94 \pm 0.04$
2.00	$0.34 \pm 0.01$	3.5	$1.12 \pm 0.10$	$0.76 \pm 0.07$	$2.17 \pm 0.03$	$1.83 \pm 0.07$
4.44	$0.21 \pm 0.01$	3.8	$0.71 \pm 0.07$	$0.62 \pm 0.12$	$1.84 \pm 0.07$	$1.33 \pm 0.08$

**Note.** The dark lane thickness ( $d_{\text{neb}}$ ), radial full width at half-maximum ( $R_{\text{FWHM}}$ ), and the radial full width at 10% of the peak ( $R_{10\%}$ ) are inferred from fitting polynomial spines to the two scattering surfaces. The uncertainties correspond to the statistical error for the different spine averaging. The  $\text{FR}_{\text{integrated}}$  column instead indicates the integrated flux ratio between both nebulae obtained using aperture photometry. We refer to the top (resp. bottom) nebula as ‘‘T’’ (resp. ‘‘B’’).

subtracting in quadrature the telescope beam size, also assumed to be Gaussian, we find that the intrinsic size of the central source is distinctly larger than the telescope beam size and increases with wavelength along the disk major axis (see Table 2). This is a unique behavior among edge-on disks, where in some cases the central star peers through the disk in the near-infrared but appears as an unresolved source.

In addition, at 7.7 and 12.8  $\mu\text{m}$ , the images show spatially extended diffuse emission extending up to radii twice that of the scattered light seen with HST and NIRCam. We assessed whether an optical problem or systematic issue might contribute to the extended appearance of the system at 7.7  $\mu\text{m}$ . A JWST optical problem can be ruled out as the origin of this for several reasons. First and most simply, the numerous background stars observed in the field surrounding Oph163131 have normal, sharply focused point-spread function (PSF) morphology in all filters. Second, the JWST wavefront sensing measurements taken on the days before and after these science observations confirm the telescope mirrors were in excellent alignment during this time period (65 nm rms telescope wavefront error in the measurement closest in time to these observations). Third, the extended nebula seen at 7.7 and 12.8  $\mu\text{m}$  is *not* aligned with JWST’s PSF hexagonal diffraction spikes, nor with MIRI’s detector short-wavelength cruciform artifact. Thus, we can rule out that any optical issue caused the extended diffuse/fluffy appearance in these 7.7 and 12.8  $\mu\text{m}$  MIRI data; the observed morphology has to be astrophysical.

Finally, we use aperture photometry to determine the flux of the source at the different wavelengths. For all filters, we use a large aperture ( $7''.5 \times 4''.5$ ) that encompasses all the emission from the source. In addition, for MIRI wavelengths, we also consider a smaller aperture ( $2'' \times 2''$ ), to illustrate the contribution from the central source. The results are reported in Table 3. The fluxes are in general agreement with the values reported in S. G. Wolff et al. (2021), but at 7.7 and 12.8  $\mu\text{m}$  our JWST fluxes are slightly higher than previous estimates from Spitzer and the Wide-field Infrared Survey Explorer (WISE).

## 4. Discussion

### 4.1. Chromaticity of the Dark Lane from 0.6 to 4.4 $\mu\text{m}$

In Section 3, we showed that the dark lane thickness decreases by a factor of 2 between 0.6 and 4.4  $\mu\text{m}$  in Oph163131 (see Table 1). This result contrasts significantly with previous JWST observations of edge-on disks showing minimal variation in dark lane thickness between the near- and mid-infrared (2–21  $\mu\text{m}$ ; Tau042021, IRAS 04302, L1527; G. Duchêne et al. 2024; M. Villeneuve et al. 2024). However,

**Table 2**  
FWHM of the Central Source at MIRI Wavelengths, Along the Disk Major Axis

$\lambda$ ( $\mu\text{m}$ )	Observed ( $''$ )	WebbPSF Model ( $''$ )	Deconvolved ( $''$ ), (au)
7.7	0.44	0.24	0.37, 54
12.8	0.65	0.45	0.47, 70
21.0	1.09	0.71	0.83, 122

**Table 3**  
Photometry of Oph163131

$\lambda$ ( $\mu\text{m}$ )	$F_{7''.5 \times 4''.5}$ (mJy)	$F_{2'' \times 2''}$ (mJy)
2.0	$6.5 \pm 0.2$	...
4.44	$2.5 \pm 0.1$	...
7.70	$2.9 \pm 0.1$	$1.6 \pm 0.1$
12.8	$3.2 \pm 0.1$	$1.9 \pm 0.1$
21.0	$35.2 \pm 1.1$	$28.5 \pm 0.9$

**Note.** We assume absolute flux calibration uncertainties of  $\sim 3\%$  based on the JWST user documentation.

other optical to near-infrared scattered light observations have also identified disks with large dark lane thickness variations between wavelengths (e.g., HK Tau B, HV Tau C. McCabe et al. 2011; Duchene et al. 2010). This suggests diversity in the structure and grain properties of protoplanetary disks, which we aim to investigate further in this section.

To interpret the wavelength variation of the dark lane thickness in Oph163131, we produce a suite of radiative transfer models with different properties, following the approach of G. Duchêne et al. (2024). The main model parameters correspond to those of model A of S. G. Wolff et al. (2021), which reproduce well the scattered light (HST) observations of the disk. That model includes an inclination of  $84.5^\circ$ , a gas scale height of 7.2 au at a radius of 100 au, a flaring exponent of 1.5, and a surface density exponent of 1.01. Following G. Duchêne et al. (2024), we adopt the DIANA dust composition (P. Woitke et al. 2016) and use the distribution of hollow spheres method (M. Min et al. 2016) to mimic compact dust aggregates. We also note that the high flaring exponent assumed here (based on previous parametric modeling of the source) should not significantly affect our qualitative analysis, as it provided the correct vertical extent at the disk outer edge, which is of interest here, in combination with the other disk parameters such as the surface density profile.

We produce six different models, which are distributed into three main families (‘‘standard,’’ ‘‘settled,’’ and ‘‘only small

**Table 4**  
Summary of Model Exploration

Model	Grain Size Distribution			Settling		Total Dust Mass ( $10^{-4} M_{\odot}$ )	Dark Lane Thickness
	$p$	$a_{\min}$ ( $\mu\text{m}$ )	$a_{\max}$ ( $\mu\text{m}$ )	$\eta_{\text{settl}}$	$a_{\text{mix}}$ ( $\mu\text{m}$ )		
Standard	3.5	0.03	1000		None	3.94	×
Dust Settling (10)	3.5	0.03	1000	0.5	10	4.59	×
Dust Settling (1)	3.5	0.03	1000	0.5	1	7.10	×
Dust Settling (0.1)	3.5	0.03	1000	0.5	0.1	1400	(✓)
Pristine Dust	3.0	0.03	0.35		None	1.94	(✓)
	1.5	0.35	100				
Only small grains	3.5	0.03	0.5		None	0.43	(✓)

**Note.** The symbols in the last column describe the degree to which a given model matches observations: a (✓) indicates a qualitatively better match, while an × symbol points to a large shortcoming of the model.

grains”). The standard model includes well-mixed grains, with sizes following a power law such that  $n(a)da \propto a^{-p}da$ , with  $p = 3.5$  and a maximum grain size of 1 mm. Three models include parametric dust vertical settling, such that grains with size  $a > a_{\text{mix}}$  have a reduced scale height of  $h(a) \propto (a/a_{\text{mix}})^{\eta_{\text{settl}}}$ , with  $\eta_{\text{settl}} = 0.5$ . We implement three scenarios where grains larger than  $a_{\text{mix}} = 10, 1, \text{ and } 0.1 \mu\text{m}$  are affected by vertical settling. Finally, we produce two models in the only small grain category. In the first one, we implement a pristine dust model with similar properties to that of G. Duchêne et al. (2024, see their Table 3 and Appendix). This model includes two power laws for the grain sizes. Grains of sizes ranging from 0.03 to  $0.35 \mu\text{m}$ , follow a power-law exponent of  $p = 3$ , while grains from  $0.35$  to  $100 \mu\text{m}$  have a power-law exponent of  $p = 1.5$ . The power laws are normalized such that 80% of the total mass is in the large grains component. The second model of this group consists of well-mixed grains, with a maximum size of  $0.5 \mu\text{m}$ . A summary of model parameters is presented in Table 4. All models are convolved by a JWST PSF obtained from the WebbPSF software (M. D. Perrin et al. 2014), and the dust mass of each model is adjusted so that its dark lane thickness at  $2 \mu\text{m}$  matches that of the observations. The comparison of the models and the data is shown in Figure 4.

As previously shown by G. Duchêne et al. (2024), we find that if grains of  $10 \mu\text{m}$  (or more) are present in the upper layers of the disk, the models show only modest chromaticity. These models do not match the observations of Oph163131. Moreover, even the models where grains larger than  $1 \mu\text{m}$  are affected by settling do not show sufficient chromaticity to reproduce the steep decrease in dark lane thickness between  $0.6$  and  $4.4 \mu\text{m}$ .

On the other hand, the model with pristine dust, the model including no grains larger than  $0.5 \mu\text{m}$ , or the model where grains larger than  $0.1 \mu\text{m}$  are affected by settling reproduces the observations better. They show a steeper curve between  $0.8$  and  $4.4 \mu\text{m}$ . This exploration suggests that the surface layers of Oph163131 are largely depleted of grains larger than  $1 \mu\text{m}$ .

Yet, we note that none of the models perfectly fit the evolution of the dark lane thickness with wavelength. Settling of grains larger than  $1 \mu\text{m}$  needs to be extremely efficient in the disk to reproduce the observations, but also, a few of those grains might still be present in the upper layers because neither the pristine dust nor the only small grain model perfectly matches the observed chromaticity. This could suggest that the settling prescription used here is too simplistic.

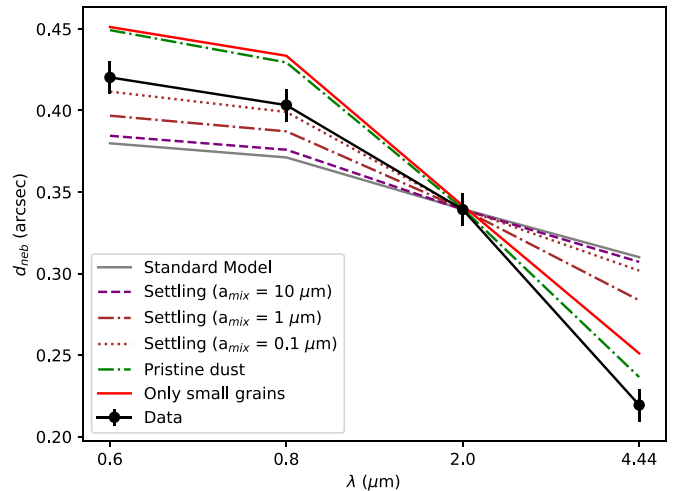


**Figure 4.** Comparison of data and radiative transfer models of the dark lane thickness as a function of wavelength. The models with grains of  $1 \mu\text{m}$  or more present in the upper layers do not show sufficient variation with wavelength to reproduce the observations.

Finally, we also found that none of the models reproduce the lateral intensity profile seen in the data, namely, that the top nebula becomes more centrally peaked at  $4.4 \mu\text{m}$  than at shorter wavelengths (Figure 1). The model where grains larger than  $0.1 \mu\text{m}$  are settled partially fits the chromaticity, but in this case, we found that the lateral intensity profile is much broader than what is observed. In this model, the surface is mostly dominated by grains smaller than the observed wavelength, and consequently, each grain shows nearly isotropic scattering with a bluish extinction opacity (Rayleigh-like scattering). To explain the observations, dust particles that exhibit forward scattering and a bluish dust opacity simultaneously would be needed. We speculate that fluffy dust aggregates consisting of small monomer grains might help, as these particles appear to have the required optical properties (R. Tazaki et al. 2019), but more detailed studies need to be performed to draw a robust conclusion.

The modeling of Oph163131 indicates that  $1 \mu\text{m}$  grains are mostly absent from the upper layers of the disk, and are at most only located below its  $\tau = 1$  surface. In other words, this indicates that grains of  $1 \mu\text{m}$  and larger are decoupled from the gas in that region. This implies that the ratio  $\alpha/\text{St}$ , where  $\alpha$  represents the turbulence level and  $\text{St}$  the Stokes number, is very low in the upper layers of the disk for these particles. Oph163131 is a well-known disk in which an extremely low

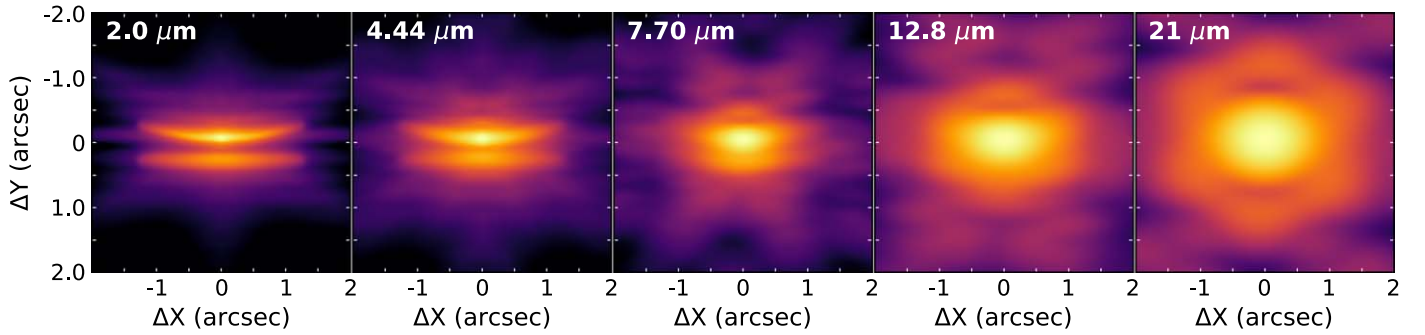


**Figure 5.** Model A from S. G. Wolff et al. (2021), including only one smooth disk region, computed at JWST wavelengths. Contrary to the data, this model does not become dominated by a central source starting at  $7.7 \mu\text{m}$  and does not include extended emission at  $7.7$  and  $12.8 \mu\text{m}$ . The fields of view of the panels showing the observations at  $7.7$ ,  $12.8$ , and  $21 \mu\text{m}$  are twice as small as those in Figure 2.

level of midplane turbulence has been identified, based on the radiative transfer modeling of its millimeter emission ( $h_g/h_{\text{mm}} > 10$ ,  $\alpha_{\text{mid}}/\text{St} \leq 6 \cdot 10^{-3}$ ; M. Villeneuve et al. 2022). The low midplane turbulence level of Oph163131 and the absence of micron-sized particles in its upper layers suggest that the overall vertical turbulence  $\alpha$  of this disk is particularly low, even at high altitude above the midplane. Alternatively, the Stokes number of particles of  $1 \mu\text{m}$  and larger may be particularly high. This could be the case if the gas surface density is very low in the upper layers of the disk, or potentially if grains are porous, as such grains have larger cross sections for the same mass, therefore increasing their Stokes number.

This result differs from those of previous studies on the variation of dark lane thickness of younger edge-on disks using JWST observations. Indeed, those showed that  $10 \mu\text{m}$  grains can be present in the upper layers of disks, even in the Class 0 stage (G. Duchêne et al. 2024; M. Villeneuve et al. 2024, Tau042021, IRAS 04302, L1527), indicative of a higher  $\alpha/\text{St}$  ratio in these disks than in Oph163131, for particles of similar sizes. All of these disks have also been studied at millimeter wavelengths, revealing different levels of vertical concentration of these large dust particles. The younger L1527 and IRAS 04302 appear vertically thick and not affected by settling (Z.-Y. D. Lin et al. 2023; M. L. R. van't Hoff et al. 2023; M. Villeneuve et al. 2023). This suggests no significant decoupling of particles up to  $\sim 1 \text{ mm}$ . At the other end, in the more evolved Class II Tau042021, dust appears settled at millimeter wavelengths (M. Villeneuve et al. 2020). This indicates that large grains eventually decouple from the gas, but for significantly larger particles ( $a \gtrsim 10 \mu\text{m}$ ) than in the case of Oph163131 ( $a \lesssim 1 \mu\text{m}$ ), possibly due to either lower turbulence, lower gas surface density, or different grain properties in Oph163131. Further statistical studies of disks at different evolutionary stages are needed to test whether such characteristics are common or if Oph163131 is an exception.

#### 4.2. The Transition in Disk Appearance Beyond $4.4 \mu\text{m}$

As shown in Section 3, the disk appearance undergoes a sharp transition beyond  $4.4 \mu\text{m}$ . Beyond this wavelength, the two reflection nebulae are not clearly visible, and the disk appearance becomes dominated by a bright central source and extended fluffy emission. The central source at MIRI wavelengths is also centered on the top scattered light nebula (see Figure 2).

The appearance of a bright and compact central source is not expected in a smooth disk, even at the inclination of

Oph163131 ( $\sim 85^\circ$ ). To illustrate this point, we computed the smooth model A of S. G. Wolff et al. (2021) at all JWST wavelengths and show the images in Figure 5. The two scattered light surfaces are dominating the source appearance up to  $21 \mu\text{m}$ , even though they are vertically unresolved at wavelengths larger than  $12.8 \mu\text{m}$ . This model does not become dominated by a bright central source starting at  $7.7 \mu\text{m}$ , contrary to the data.

To explain the significant change of morphology with wavelengths, several configurations are possible. For instance, a drastic change in the dust scattering properties, leading to almost exclusively forward scattering at  $7.7 \mu\text{m}$ , might lead to such an important change in the disk morphology. This might, for example, happen if the observations at  $7.7 \mu\text{m}$  probe significantly larger grains than those seen at  $4.4 \mu\text{m}$  but it is difficult to reconcile with our current understanding of dust properties and dust settling. Alternatively, the inner disk could become suddenly very bright at  $7.7 \mu\text{m}$  and directly visible such that it dominates over the outer disk brightness. This can be expected if the inner disk is tilted above the outer disk or in the case of a very vertically and optically thick inner disk, which could be seen through the outer disk as the latter became optically thin. In this section, we produce a toy model using radiative transfer to test this second option.

The goal of our toy model is to test whether a vertically and optically thick inner disk could produce the observed change in morphology, and specifically, the appearance of a compact source and the disappearance of the scattering nebulae starting from  $7.7 \mu\text{m}$ . We modified model A from S. G. Wolff et al. (2021) such that the inner  $10 \text{ au}$  contain as much mass as the outer  $100 \text{ au}$  of the disk ( $M_{\text{dust}} = 5 \cdot 10^{-4} M_\odot$ ), and such that the scale height is approximately four times larger within  $10 \text{ au}$  than at larger radii. This transition radius roughly corresponds to the size of the very bright inner region detected in millimeter wavelengths (about five times brighter than the rest of the disk). In the modeling of the Atacama Large Millimeter/submillimeter Array (ALMA) observations, M. Villeneuve et al. (2022) obtained a surface density more than one order of magnitude higher in that inner region than in the rest of the disk, providing support to the toy model scenario presented here. The millimeter dust height in this region was however not constrained with ALMA. The model images are convolved by the JWST PSF and are shown in Figure 6.

We find that this model is able to produce a sharp transition in the shape of the source between  $4.4$  and  $7.7 \mu\text{m}$ . At  $4.4 \mu\text{m}$ , in addition to the two scattering nebulae, there is a hint of the diffraction from the PSF, suggesting that a bright source starts



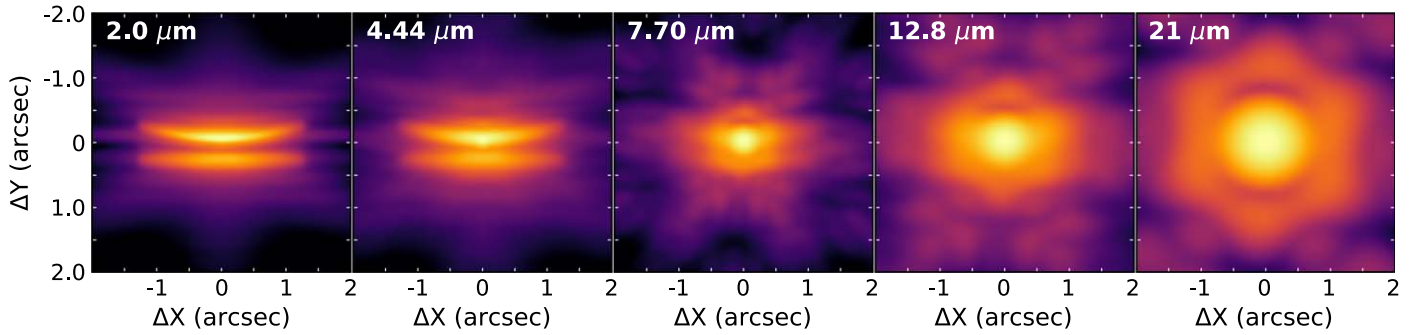


**Figure 6.** Toy model including a very massive and vertically thick inner region, allowing to reproduce a sharp transition in the source appearance beyond  $4.4 \mu\text{m}$ . The fields of view of the panels showing the observations at  $7.7$ ,  $12.8$ , and  $21 \mu\text{m}$  are twice as small as those in Figure 2. The compact source appearing at  $7.7 \mu\text{m}$  and longer wavelengths is not centered on the position of the star in the model, but offset by  $20 \text{ mas}$  or more toward the upper nebulae.

to shine through, which is also seen in the data. Then, starting at  $7.7 \mu\text{m}$ , the emission becomes dominated by the inner top scattering surface, which starts to scatter significantly. Indeed, at all wavelengths, the brightest pixel in the model image is offset by more than  $20 \text{ mas}$  from the position of the star, which shows that the bright central emission does not correspond to the star itself. Consistent with observations, the spectral energy distribution of the model shows a sharp rise beyond  $10 \mu\text{m}$ , while the main morphological changes occur between  $4.44$  and  $7.7 \mu\text{m}$ , which also supports this interpretation.

Enhancing both the mass and scale height of the inner disk in the model creates a sharp transition at  $10 \text{ au}$ , where photons from the inner disk must first scatter very high up above the midplane before being directed toward the outer disk. The line of sight from the observer to that location goes through relatively little column density in the outer disk, and that line of sight becomes optically thin between  $4.4$  and  $7.7 \mu\text{m}$ , hence the behavior of the model images. In other words, the compact central source can be interpreted as emission from the star and the inner disk that is not seen directly, but which instead is able to progressively propagate through the disk to greater distances at longer wavelengths.

Finally, we note that the central source in the model is not resolved, nor does its size increase with wavelengths, as seen in the data. The apparent deconvolved size of the central source in the data, along the major axis of the disk, goes from  $54$  to  $122 \text{ au}$  between  $7.7$  and  $21 \mu\text{m}$  (Table 2), which roughly corresponds to the location of the two rings modeled in the ALMA continuum observations (M. Villeneuve et al. 2022). However, at these wavelengths, thermal emission is expected to arise from within  $5 \text{ au}$ , which is significantly smaller than the observed sizes. This supports the interpretation that the compact central source seen at MIRI wavelengths does not correspond to direct thermal emission but instead to scattered photons that were thermally emitted and are able to propagate further in the disk. Further modeling would be required to quantitatively explore the conditions for such behavior.

#### 4.3. The Nature of the Patchy Extended Emission

At  $7.7$  and  $12.8 \mu\text{m}$ , the observed scattered light images show a significant contribution from extended emission (Figure 2). This feature does not appear axisymmetric and potentially includes a dark, apparently shadowed region extending outward along the midplane, southwest and northeast of the source. In Figure 7, we overlay the MIRI  $7.7 \mu\text{m}$  image with the millimeter continuum and  $^{12}\text{CO}$  gas emission probed by ALMA. We find that the extended and faint emission is

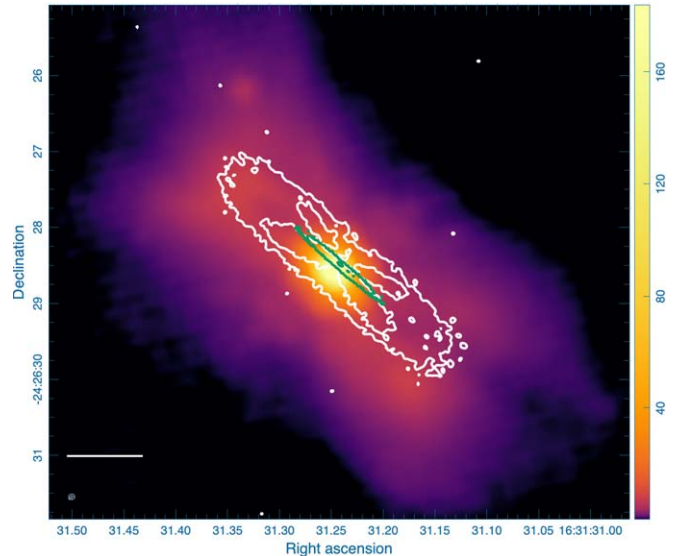


**Figure 7.** Overlay MIRI  $7.7 \mu\text{m}$  image, using the same color scale as in Figure 2, and ALMA  $1.3 \text{ mm}$  dust continuum (green contours, with levels  $10\sigma_{\text{cont}}$  and  $20\sigma_{\text{cont}}$ ) and  $^{12}\text{CO}$  observations (white contours, with levels  $5\sigma_{\text{CO}}$  and  $20\sigma_{\text{CO}}$ ), illustrating that the fluffy emission is located at higher altitude and larger radii than the gas emission. The ALMA data were published in M. Villeneuve et al. (2022). A  $1''$  scale is represented by a horizontal line in the bottom left corner of the figure.

detected from the disk midplane to above the molecular disk as traced in CO. It is also extended to larger radii than the  $^{12}\text{CO}$  emission. The origin of this emission is currently unknown. It is, however, unlikely to be thermal continuum emission across the broad F770W and F1280W bandpasses, as any dust grains in the region would be expected to also produce scattered light signatures at other wavelengths, which are not observed.

Intriguingly, an extended feature had previously been detected in JWST images of the Class II edge-on disk Tau042021. In that source, the extended feature was detected in the same JWST broadband filters as in Oph163131, centered on  $7.7$  and  $12.8 \mu\text{m}$ , in the form of a sharp X-shape (G. Duchêne et al. 2024). Using MIRI/MRS observations, N. Arulanantham et al. (2024) revealed that the X-shape feature in Tau042021 corresponds to  $\text{H}_2$  and PAH line emission. This could be indicative of a disk wind lifting material above the disk surface and of shocks exciting the lines.

In the case of Oph163131, the patchy emission is confined to a region much closer to the disk surface (i.e., with a larger opening angle compared to the minor axis direction than in



Tau042021), and lacks sharp-edge features indicative of shocks. Photoexcitation or stochastic heating of material surrounding the source might explain the extended structure that we observe. However, given the lack of spectral signatures of accretion in Oph163131 (C. Flores et al. 2021), the flux of high-energy photons from the central source should be much weaker than in Tau042021. Yet, the relatively symmetric appearance of the extended emission around the source and the suggestive disk shadow extending out into the patchy emission along the disk plane (Figure 2) suggests that the central source is illuminating the extended emission. Even though Oph163131 is not located in a PAH-bright region in the Spitzer IRAC Channel 4 maps, illumination by an external UV field, already suggested by C. Flores et al. (2021) to explain the vertically isothermal profile in  $^{12}\text{CO}$  observations outside of 300 au, is a possible alternative explanation.

## 5. Conclusion

We presented new JWST images of the Class II disk Oph163131. The two scattering surfaces of the disk are well visible up to  $4.4\ \mu\text{m}$ . At longer wavelengths, the disk reveals a drastically different morphology. A compact source suddenly appears between  $4.4$  and  $7.7\ \mu\text{m}$ , larger than the JWST PSF along the disk major axis, and increasing in size between  $7.7$  and  $21\ \mu\text{m}$ . Moreover, extended patchy emission is visible at  $7.7$  and  $12.8\ \mu\text{m}$ , extending twice as far as the scattered light disk seen at shorter wavelengths.

We find a significant decrease in dark lane thickness by a factor of  $\sim 2$  between  $0.6$  and  $4.4\ \mu\text{m}$ , which is consistent with no grains larger than about  $1\ \mu\text{m}$  in the upper layers of the disk. For these particles, this implies that vertical settling dominates over dust stirring, keeping them below the  $\tau = 1$  surface. This could be explained by low turbulence up to high altitude above the disk midplane. This result however contrasts with constraints from younger sources with previous JWST observations, where larger grains of  $10\ \mu\text{m}$  remained coupled to the gas and present in the disk's upper layers. This points to a diversity in vertical settling/dust stirring efficiency between disks, which needs to be further explored.

The compact central source visible from  $7.7\ \mu\text{m}$  is interpreted as emission from the star and inner disk that is not seen directly but scattered at progressively larger distances at longer wavelengths. We present a toy model that can produce the sudden transition from parallel linear nebulae to a compact central source, which employs a very vertically and optically thick inner disk. The model however does not reproduce the size increase in the compact emission with wavelength.

The nature of the extended patchy emission is unclear, but the lack of sharp-edged structures argues against the presence of shocks and suggests instead photoexcitation or stochastic heating of material smoothly flowing away from the star along the disk surface. Additional modeling and JWST IFU measurements will be needed to fully understand the wavelength evolution of this remarkable system.

## Acknowledgments




M.V. thanks Giovanni Rosotti for the useful discussions. A portion of this research was carried out at the Jet Propulsion Laboratory, California Institute of Technology, under a contract with the National Aeronautics and Space Administration

(80NM0018D0004). The research of M.V. was conducted in a large fraction and supported by an appointment to the NASA Postdoctoral Program at the NASA Jet Propulsion Laboratory, administered by Oak Ridge Associated Universities under contract with NASA. This project has received funding from the European Research Council (ERC) under the European Union's Horizon Europe research and innovation program (grant agreement No. 101053020, project Dust2Planets, PI: F. Ménard and grant agreement No. 101039651, project DiscEvol, PI G. Rosotti). Views and opinions expressed are, however, those of the author(s) only and do not necessarily reflect those of the European Union or the European Research Council. Neither the European Union nor the granting authority can be held responsible for them. M.V., K.R.S., G.D., and S.G.W. acknowledge funding support from JWST GO program #2562 provided by NASA through a grant from the Space Telescope Science Institute, which is operated by the Association of Universities for Research in Astronomy, Incorporated, under NASA contract NAS5-26555. The JWST data presented in this article were obtained from the Mikulski Archive for Space Telescopes (MAST) at the Space Telescope Science Institute. The specific observations analyzed can be accessed at the following doi:10.17909/zrsp-nc48. This paper makes use of the following ALMA data: ADS/JAO.ALMA#2018.1.00958.S and 2016.1.00771.S, which were observed with the band 6 receivers (G. A. Ediss et al. 2004; A. R. Kerr et al. 2014).

*Facilities:* JWST, HST, ALMA.

*Software:* mcfost (C. Pinte et al. 2006, 2009), matplotlib (J. D. Hunter 2007), NumPy (C. R. Harris et al. 2020), photutils (L. Bradley et al. 2024), CARTA (A. Comrie et al. 2021).

## ORCID iDs

Marion Villenave  <https://orcid.org/0000-0002-8962-448X>  
 Karl R. Stapelfeldt  <https://orcid.org/0000-0002-2805-7338>  
 Gaspard Duchêne  <https://orcid.org/0000-0002-5092-6464>  
 François Ménard  <https://orcid.org/0000-0002-1637-7393>  
 Marshall D. Perrin  <https://orcid.org/0000-0002-3191-8151>  
 Christophe Pinte  <https://orcid.org/0000-0001-5907-5179>  
 Schuyler G. Wolff  <https://orcid.org/0000-0002-9977-8255>  
 Ryo Tazaki  <https://orcid.org/0000-0003-1451-6836>  
 Deborah L. Padgett  <https://orcid.org/0000-0001-5334-5107>

## References

- Arulanantham, N., McClure, M. K., Pontoppidan, K., et al. 2024, *ApJL*, **965**, L13
- Baumann, M., Boch, T., Pineau, F.-X., et al. 2022, in ASP Conf. Ser. 532, *Astronomical Data Analysis Software and Systems XXX*, ed. J. E. Ruiz, F. Pierfederci, & P. Teuben (San Francisco, CA: ASP), **7**
- Benisty, M., Dominik, C., Follette, K., et al. 2023, in ASP Conf. Ser. 534, *Protostars and Planets VII*, ed. S. Inutsuka et al. (San Francisco, CA: ASP), **605**
- Birnstiel, T., Klahr, H., & Ercolano, B. 2012, *A&A*, **539**, A148
- Bonnarel, F., Fernique, P., Bienaymé, O., et al. 2000, *A&AS*, **143**, 33
- Bradley, L., Sipocz, B., Robitaille, T., et al. 2024, *astropy/photutils: 2.0.2*, Zenodo, doi:10.5281/zenodo.596036
- Burrows, C. J., Stapelfeldt, K. R., Watson, A. M., et al. 1996, *ApJ*, **473**, 437
- Comrie, A., Wang, K.-S., Hsu, S.-C., et al. 2021, CARTA: The Cube Analysis and Rendering Tool for Astronomy v4.0.0, Zenodo, doi:10.5281/zenodo.4905459
- Cotera, A. S., Whitney, B. A., Young, E., et al. 2001, *ApJ*, **556**, 958
- Duchêne, G., McCabe, C., Pinte, C., et al. 2010, *ApJ*, **712**, 112
- Duchêne, G., Ménard, F., Stapelfeldt, K. R., et al. 2024, *AJ*, **167**, 77

- Ediss, G. A., Carter, M., Cheng, J., et al. 2004, in Fifteenth Int. Symp. on Space Terahertz Technology (*Northampton, MA*) ed. G. Narayanan, [181](#)
- Evans, N. J., II, Dunham, M. M., Jørgensen, J. K., et al. 2009, [ApJS](#), **181**, [321](#)
- Facchini, S., Lodato, G., & Price, D. J. 2013, [MNRAS](#), **433**, [2142](#)
- Flores, C., Duchêne, G., Wolff, S., et al. 2021, [AJ](#), **161**, [239](#)
- Gaia Collaboration, Brown, A. G. A., Vallenari, A., et al. 2021, [A&A](#), **649**, [A1](#)
- Harris, C. R., Millman, K. J., van der Walt, S. J., et al. 2020, [Natur](#), **585**, [357](#)
- Hunter, J. D. 2007, [CSE](#), **9**, [90](#)
- Kerr, A. R., Pan, S.-K., Claude, S. M. X., et al. 2014, [ITTST](#), **4**, [201](#)
- Kuffmeier, M., Dullemond, C. P., Reissl, S., & Goicovic, F. G. 2021, [A&A](#), **656**, [A161](#)
- Lambrechts, M., & Johansen, A. 2012, [A&A](#), **544**, [A32](#)
- Lin, Z.-Y. D., Li, Z.-Y., Tobin, J. J., et al. 2023, [ApJ](#), **951**, [9](#)
- McCabe, C., Duchêne, G., Pinte, C., et al. 2011, [ApJ](#), **727**, [90](#)
- Min, M., Rab, C., Woitke, P., Dominik, C., & Ménard, F. 2016, [A&A](#), **585**, [A13](#)
- Perrin, M. D., Sivaramakrishnan, A., Lajoie, C.-P., et al. 2014, [Proc. SPIE](#), **9143**, [91433X](#)
- Pinte, C., Harries, T. J., Min, M., et al. 2009, [A&A](#), **498**, [967](#)
- Pinte, C., Ménard, F., Duchêne, G., & Bastien, P. 2006, [A&A](#), **459**, [797](#)
- Stapelfeldt, K. R., Duchêne, G., Perrin, M., et al. 2014, in *Exploring the Formation and Evolution of Planetary Systems*, Vol. 299 ed. M. Booth, B. C. Matthews, & J. R. Graham, [99](#)
- Tazaki, R., Ménard, F., Duchêne, G., et al. 2024, [ApJ](#), (submitted)
- Tazaki, R., Tanaka, H., Muto, T., Kataoka, A., & Okuzumi, S. 2019, [MNRAS](#), **485**, [4951](#)
- van't Hoff, M. L. R., Tobin, J. J., Li, Z.-Y., et al. 2023, [ApJ](#), **951**, [10](#)
- Villenave, M., Ménard, F., Dent, W. R. F., et al. 2020, [A&A](#), **642**, [A164](#)
- Villenave, M., Podio, L., Duchêne, G., et al. 2023, [ApJ](#), **946**, [70](#)
- Villenave, M., Stapelfeldt, K. R., Duchêne, G., et al. 2022, [ApJ](#), **930**, [11](#)
- Villenave, M., Stapelfeldt, K. R., Duchêne, G., et al. 2024, [ApJ](#), **961**, [95](#)
- Watson, A. M., & Stapelfeldt, K. R. 2004, [ApJ](#), **602**, [860](#)
- Watson, A. M., Stapelfeldt, K. R., Wood, K., & Ménard, F. 2007, in *Protostars and Planets V*, ed. B. Reipurth, D. Jewitt, & K. Keil, [523](#)
- Woitke, P., Min, M., Pinte, C., et al. 2016, [A&A](#), **586**, [A103](#)
- Wolf, S., Padgett, D. L., & Stapelfeldt, K. R. 2003, [ApJ](#), **588**, [373](#)
- Wolff, S. G., Duchêne, G., Stapelfeldt, K. R., et al. 2021, [AJ](#), **161**, [238](#)
- Youdin, A. N., & Lithwick, Y. 2007, [Icar](#), **192**, [588](#)